Species and Temperature Measurement in H_2/O_2 Rocket Flow Fields by Means of Raman Scattering Diagnostics

Wim A. de Groot*
Sverdrup Technology, Inc.
NASA Lewis Research Center Group
Brookpark, Ohio 44142

Jonathan M. Weiss**
Propulsion Engineering Research Center
Department of Mechanical Engineering
The Pennsylvania State University
University Park, PA 16802

Abstract

Validation of Computational Fluid Dynamic (CFD) codes developed for prediction and evaluation of rocket performance is hampered by a lack of experimental data. Non-intrusive laser based diagnostics are needed to provide spatially and temporally resolved gas dynamic and fluid dynamic measurements. This paper reports the first non-intrusive temperature and species measurements in the plume of a 110 N gaseous hydrogen/oxygen thruster at and below ambient pressures, obtained with spontaneous Raman spectroscopy. Measurements at 10 mm downstream of the exit plane are compared with predictions from a numerical solution of the axisymmetric Navier-Stokes and species transport equations with chemical kinetics, which fully model the combustor-nozzle-plume flowfield. The experimentally determined oxygen number density at the centerline at 10 mm downstream of the exit plane is four times that predicted by the model. The experimental number density data fall between those numerically predicted for the exit and 10 mm downstream planes in both magnitude and radial gradient. The predicted temperature levels are within 10 to 15% of measured values. Some of the discrepancies between experimental data and predictions result from not modeling the three dimensional core flow injection mixing process, facility back pressure effects and possible diffuser-thruster interactions.

Nomenclature

A_{exit}	Exit plane cross sectional area
A_{throat}	Throat cross sectional area
c	Velocity of light (2.9979 x 10^8 m/sec)
C	Optical efficiency factor
C_{vib}	Vibrational relaxation constant 5.42×10^{-5} atm.μsec)
$E_{J,v,ini}$	Initial molecular rotational-vibrational energy
g_n	Nuclear spin degeneracy
h	Planck's constant (6.63 x 10^{-34} Joule.sec)
I_{las}	Laser intensity
$I_{sc,ob}$	Observed scattering intensity
J	Rotational quantum number
k	Boltzmann's constant (1.38 x 10^{-23} Joule/K)
K_2	Vibrational relaxation factor (2.95×10^6 K)
m	Molecular mass
N	Total species number density
$N_{J,v}$	Number density in energy level given by J,v
p	Pressure
S_J	Teller-Placzek coefficient
T	Temperature
v	Vibrational quantum number
$Z_{J,v}$	Partition function of initial state
$\alpha'_{ini,fin}$	Terms of the derived polarizability tensor
θ	Angle between incident and collection optics
λ_{las}	Laser wavelength
λ_{tr}	Molecular mean free path length

---

* Aerospace Engineer, Member AIAA.

** Graduate Research Assistant, Student Member AIAA.

ν_{las}	Laser light frequency
ν_{RS}	Raman shift
σ_{Raman}	Raman scattering cross section
τ_{rot}	Rotational relaxation time
τ_{tr}	Translational relaxation time
τ_{vib}	Vibrational relaxation time
Ω	Solid angle of collection optics

Introduction

Designers of future NASA and commercial spacecraft require improved auxiliary (onboard) propulsion systems. The benefits of higher performance include increases in revenue-producing lifetime[1] and/or increases in mission capabilities by allowing greater payloads through a reduced propellant mass. Depending on their specific task, e.g. reaction control, drag makeup, orbit maneuver or station keeping, such propulsion systems need to provide thrust levels from 1 to 1000 N. To improve the performance of these systems, it is necessary to better understand the energy loss mechanisms, which include mixing and vaporization efficiencies (liquid injectors), boundary layer and heat transfer losses, reaction kinetic losses and two-dimensional losses. CFD-models have been developed to include these losses in the prediction and analysis phase of chemical rocket design. Recommended procedures to utilize these CFD-models in the performance prediction and evaluation of liquid rocket engines have been documented in the JANNAF methodology manuals.[2] This methodology has been standardized and proven invaluable to the rocket community.

Traditionally, low thrust rocket designers have used the same prediction methodology in their design process as for larger rockets. This approach leads to inaccurate predictions when applied to certain low thrust rockets. For example, there was an approximate ten percent overprediction of specific impulse for gaseous H/O, 110-220 N rockets with fuel film cooling,[3,4] the specific causes of which were not identified.

In order to improve the design process of small rockets, experimental efforts combined with numerical analyses are underway to study the effects of combustor mixing and low Reynolds numbers on the prediction of small thruster flowfields and the evaluation of their performance. Towards this end, a numerical flow code which solves the axisymmetric Navier-Stokes and species transport equations with finite rate chemistry, referred to as RK/PLUS, is developed and used to model the engine flowfield from the entrance of the combustion chamber through the nozzle and into the plume. This code consistently underpredicts measured performance by 4% and chamber pressures by about 10% over a range of O/F ratios.[5] A probable source of this inaccuracy is the inability of the model to predict three-dimensional mixing effects between the hydrogen film coolant and the core combustion gases. Studies show[6] that the shape of the splitter plate between the fuel film and the core gas affects the shear layer mixing and as a result the overall performance. To complicate the assessment, this effect varies with varying fuel film cooling percentage.

A schematic of the flowfield of the 110 N, regeneratively cooled gaseous hydrogen/oxygen thruster is shown in Fig. 1. The percentage of fuel that is needed for film cooling is between 60% and 75%. The remainder of the fuel is injected through a platelet injector into the core region. During ignition, a sparkplug in the center excites the oxygen which then reacts with the hydrogen. After ignition, combustion is sustained in the bluff body recirculation region behind the sparkplug tip, where velocities are relatively low and good turbulent mixing takes place. This primary combustion zone causes an oxygen rich product mixture to emerge from the injector. The splitter plate between the fuel film and this oxygen rich core generates a secondary combustion shear layer where the fuel and oxygen mix and react. To achieve full wall protection, the film should be sufficiently thick to maintain wall coverage through the throat. This can result in a hydrogen rich boundary layer throughout the nozzle.

Several experimental diagnostics methods are being employed to measure rocket and flow variables and to anchor and validate codes. Spectrally resolved Rayleigh[7,8] scattering measurements are used to measure temperature and velocities in the exit plane of a regeneratively cooled rocket with an expansion ratio of 30. This paper reports the application of spontaneous Raman scattering for the measurement of species and temperature in flow field areas where the number densities of the species are sufficiently high ($> 10^{17}$ /cm^3) to be measured by this technique and where optical access allows it to be applied. Unique to this system is the application of optical fibers for access to the flowfield in conjunction with high power pulsed lasers (1 Joule/pulse). The reason for using these fibers and their advantage will be discussed. As

an indication of the RK/PLUS performance, some comparisons are presented between RK/PLUS flow predictions on an expanding plume outside a shortened nozzle and measurements taken by means of spontaneous Raman scattering. A shortened nozzle is selected for the number densities to be high enough to be detected. Furthermore, concentration and temperature profiles on this shortened nozzle allow some conclusions to be drawn on the chamber mixing and combustion processes.

Raman Scattering Diagnostics

Raman scattering for the measurement of combustion species and temperature has become popular over the last two decades. The strength of Raman scattering lies in the linear relationship between the scattered intensity and the number density which makes the interpretation of the scattered spectrum quite straightforward. High power lasers makes the use of this technique possible even at ambient pressures. A summary treatise on the Raman scattering theory has been given by Long.[9] For reference, a summary is given in Appendix A. Lederman[10] and Lapp and Penney[11,12] were some of the first researchers to put this theory to practical application for combustion gasdynamics research.

There are several approaches to the use of Raman scattering for determination of species number densities and temperatures. At higher temperatures, higher vibrational states are populated. This makes the transition from a higher to a lower vibrational state more likely, giving rise to the anti-Stokes scattering band. If both Stokes and anti-Stokes transition bands are measured simultaneously, the temperature can be extracted from the ratio of their intensities (integrated over the full rotational-vibrational transition). The intensity of the Stokes line can then be used to determine the species number densities. Dibble and co-workers used this technique in hydrogen-air[13] and methane-air[14] flames. Due to its dominant presence, nitrogen was used to measure the temperature by means of Stokes/anti-Stokes ratio. This temperature was then used to extract the number densities of all major species whose Stokes line intensities are measured simultaneously with a polychromator/photomultiplier tube assembly.

Since the population distribution of the molecules over the rotational energy states depends on the temperature, measuring a pure rotational band will also give the temperature from the intensity distribution. As it is difficult to resolve the rotational lines of most species (the O- and S-branch are too weak and the Q-branch too close together), this technique is usually reserved for hydrogen species at higher pressures,[15] because lines of hydrogen are farther apart and its scattering cross section is large compared with most species.

The population distribution of the molecules over the rotational levels within one vibrational transition depends on temperature and at these densities can be calculated from the Boltzman distribution. Similarly, the population over the different vibrational levels can be calculated. At higher temperatures, the higher vibrational levels become more populated and the transitions originating from these higher vibrational levels become more distinct. The temperature can be extracted by curvefitting a measured vibrational Q-branch with the calculated Q-branch. The species densities can be extracted from the temperature and integrated Q-branch intensity after some calibration measurements.[16]

Due to the low number densities and relatively poor wavelength resolution, the first two approaches can not be applied in the current facility. The chosen approach is the Q-branch profiling. This paper presents some low number density and temperature results obtained with vibrational Q-branch profiling of O_2 in the plume of a rocket with shortened nozzle.

Experiment

Rocket Facility

These tests were performed in the low thrust rocket test facility[17] at the NASA Lewis Research Center. The facility has a continuous high altitude capability and is used for life and performance testing of gaseous H_2/O_2 rockets in the 2-200 N thrust classes. It consists of an altitude chamber of 0.9 m diameter and 1.8 m length which is evacuated to high altitude conditions ($\sim$ 1000 Pa) by means of a stack of two air driven ejectors. A horizontal thrust stand holds the rocket and measures the thrust. Together with the measured propellant mass flow rates and chamber pressure, these parameters enable the calculation of experimental I_{sp} and C^* for a given rocket. The plume of the rocket is captured by a supersonic, watercooled diffuser and is evacuated through the ejectors after being cooled down in a water spray cart.

The low area ratio research rocket, shown in a cross-sectional view in Fig. 2 is installed for this experiment. It consists of a watercooled combustion chamber of 0.025 m diameter and 0.102 m length, milled out of OFHC copper. The rocket is fitted with an Aerojet stacked platelet injector.[3] A sleeve insert extends 0.050 m into the chamber and provides hydrogen film cooling. The nozzle was terminated at an area ratio A_{exit}/A_{throat} of 1.855. The hydrogen film that is injected through the sleeve has a lower temperature than the regeneratively heated hydrogen film since water is used for wall cooling. Consequently, the injection velocity of the fuel film and hence the film to core velocity ratio of the research rocket will be less than in the regeneratively cooled chamber. The effect of this velocity ratio is unknown.

For this experiment, the mass mixture ratio oxygen/hydrogen was 5.13. A film cooling percentage of 75% was used as in the regeneratively cooled chamber. Combustion chamber pressure was 0.5 MPa. During testing it was found that moving the diffuser far enough from the thruster exit plane to provide optical access resulted in rapid hydrogen build-up in the tank. Hydrogen accumulation therefore limited each test to about 30 seconds.

Raman Facility

The Raman facility consists of a flashlamp pumped dye laser with fiber optic transmission, fiber optic signal transmission and signal detection by a spectrometer/photomultiplier combination.
The design of the Raman facility was governed by facility constraints and is fully described in Ref. 18. Several changes had to be made to this early design to accommodate low number density measurements. A 0.5 m spectrometer replaced the triplemate spectrometer. This resulted in an increase in light throughput by a factor of five. The linear array was replaced by a photomultiplier tube. The resulting setup is shown in Fig. 3. Safety requirements dictate that the rocket test facility be vented. Large volumes of outside air are drawn into the test facility through access doors and out through ceiling fans to prevent possible accumulation of hydrogen. Large temperature fluctuations and amounts of dust exist within the engine test cell facility. The Raman facility is therefore located in a separate room adjacent to the testcell. The room is kept at constant humidity and temperature.

Laser: A flashlamp pumped dye laser is used to excite the molecules. The laser provides 1 Joule/pulse at a pulse rate of 10 Hz. The dye used is Rhodamine 590 (Rh 6G), with a maximum energy output at 599 nm. The pulse length is 2 μsec and the beam diameter 6 mm. For Raman scattering, high laser energy is required since the signal strength is weak. However, high energy over a short (10^{-8} sec) time pulse means a high average power. This can lead to gas breakdown or the appearance of stimulated Raman scattering, processes that affect the scattering phenomenon and interfere nonlinearly with the observed process. A longer pulselength means a lower power which averts these undesired processes. The disadvantage of longer pulselength is that the Kolmogorov time scale will not be satisfied,[19] which means that only time averaged measurements can be made and not time resolved measurements. Laser pulse energy was measured directly with a laser energy meter.

Fibers: The long pulselength or low average pulse power of the laser enables it to be coupled into an optical fiber. With laser wavelength in the visible range of the spectrum, the loss in pulse energy (transmission > 99.6 % per m) is negligible for short lengths of fiber. To the authors knowledge, the only other researchers to use optical fibers in Raman thermometry were Shirley and Chin[20] who coupled a 10 Watt cw Argon-Ion laser in a 50-100 μm fiber to measure temperature in the SSME preburner, at high gas pressures of 14 - 42 MPa. Pressures in the current experiment range from 0.5 MPa in the combustor to 0.01 MPa in the plume, excluding the use of CW lasers.

Optical fibers are used to transport laser pulses to the experiment and scattered light back to the diagnostics room. A periscope system was ruled out because of the large transmission distances, lack of facility temperature control, and lack of clean room conditions. A 20 m long, 800 μm diameter fiber with a Numerical Aperture (N.A.) of 0.22 is used for laser pulse transport. An epoxy-free microscope objective is used to couple the 6 mm diameter beam into the fiber. The space between the objective and fiber is purged with nitrogen to prevent damage due to dust accumulation. Ceramic high power SMA 905 connectors are used for laser-fiber coupling. Metal connectors cause the fiber to crack on the surface, probably due to unequal thermal expansion between the fiber, the epoxy that holds the fiber in the connector

and the stainless connector.

Careful laser-fiber alignment is required. The laser beam intensity profile has to be homogeneous, preferably a Gaussian shape, as long as no high energy "hot spots" occur. A laser fiber coupler is used for alignment. Focusing the laser beam slightly ahead of the fiber face such that the beam expands while entering the fiber will improve the chance of fiber survival. Focusing the beam on the fiber surface or misaligning the beam causes fiber surface damage. Figures 4a and b show undamaged and damaged fiber surfaces. These figures reveal improper laser alignment as well as damage caused by focusing the beam on the fiber surface causing 'pitting'.

The fiber damage problem was eliminated by painting the front of a solid metal SMA 905 connector black and using the burn pattern to properly focus and align the laser. A single laser pulse burns off the paint, from which an approximate focusing and alignment can be determined. The solid SMA connector can subsequently be replaced with the connector holding the fiber. After proper alignment has been achieved, >75% of the laser energy is coupled into the fiber. The fiber transports the laser pulse from the laser through the bulkhead of the altitude chamber and delivers the pulse to the test rocket where a lens refocuses the light emerging from the fiber with a 1:1 magnification into the plume. The emerging laser beam is captured with a beam dump to reduce noise from stray light.

Receiving optics: A receiving lens with an effective f# of 3.2 is used to collect Raman scattered light at an angle of 90° from the incident laser. A second lens is used to couple the collected light into another 800 μm fiber with a N.A. of 0.22. The positions of the collection and reimaging lenses give a 1:1 magnification. Accordingly, the measurement probe volume has a length of 800 μm. The signal fiber delivers the collected light into the laser room, where a lens collimates the light emerging from the fiber. Collimated light is needed for a Raman notch filter to work optimally. The notch filter has an effective attenuation at the laser wavelength of 10^{-6}. This filters out virtually all stray light from the laser that has entered the receiving optics. A focusing lens focuses the light into a 0.5 m spectrometer. The spectrometer has a f# of 4.0 and high stray light rejection.

Detection equipment: The spectrometer is equipped with a 1200 groove grating. This gives a dispersion of 1.6 nm/mm. With the usual exit slit width of 2 mm this means an integration over the energy emitted over 3.2 nm spectral width. A photomultiplier tube with a quantum efficiency of 5% at 680 nm is installed at the exit plane. The signal from the photomultiplier tube is amplified through a high frequency preamplifier (300 MHz bandwidth) and the resulting signal is processed by a gated integrator and boxcar averager. A 400 MHz bandwidth storage oscilloscope is used to observe the timing and signals.

Data Acquisition and Processing.

As mentioned in the rocket facility description, each test run of the research rocket is limited to 30 seconds. With a laser pulse frequency of 10 Hz this means that 300 pulsed measurements are taken for each test run. Each scattered pulse is processed separately by the boxcar averager. Accordingly, the scattered intensity is integrated over the length of the pulse by imposing a gate signal. This integrated intensity represents the total energy scattered from one laser pulse. Each series of 300 pulses is stored as a time sequence in the memory of a 386/25 personal computer. The laser pulse energy is simultaneously measured and stored and used to correct the data for pulse-to-pulse variation in laser energy.

The measurement method used is a total vibrational Q-branch curve fit. Figure 5 shows measurements of the vibrational Q-branch of oxygen in ambient air and of oxygen in the plume of the low area ratio research rocket. Due to the fact that the laser line bandwidth is wide compared to the vibrational band spacing of oxygen, some of the vibrational structure is lost. The number densities to be measured require the use of a 2 mm wide spectrometer slit to achieve acceptable signal to noise ratio on the photomultiplier tube. This means that the spectral intensity is integrated over 3.2 nm of the spectrum. After each measurement, the grating is advanced 1.0 nm and a new measurement is obtained.

A spectral scan of the oxygen Q-branch is performed in ambient air for each spatial location. With the known number density and temperature, calibration factors are obtained by curvefitting a theoretical spectrum with the measured spectrum. The curve fit routine used is a chi-square curve fit routine with multiple variables according to the Levenberg-Marquardt[21] method. The calibration factors are the

vertical offset, caused by stray light and electronic noise, the horizontal shift, due to the uncertainty in laser line location, the laser line width (given by the full width at half maximum) and the scale factor, to convert theoretical energy to measured voltage. These calibration factors are determined from the ambient conditions and used in the curvefit for the high temperature measurements. Temperature and number densities of oxygen are extracted from this curve fit.

To measure hydrogen and water number densities and temperature one would ideally calibrate in situ with a cell of known hydrogen concentration and temperature. Since this is not available, measurements of hydrogen and water involves an additional correction. The instrument function of the spectrometer and the quantum efficiency of the photomultiplier tube have to be determined for the spectral range of interest. The reference spectrum from which calibration factors are obtained for these measurements is the ambient nitrogen Q-branch. The nitrogen number density in ambient air is high (2×10^{19} /cm^3) and is concentrated in the vibrational groundstate, giving a strong signal.

Results

A radial traverse at 10 mm downstream of the exit plane measuring temperature and oxygen number density was completed. Curve fits with high accuracy were obtained in the core region where relatively high number densities were found. However, it was difficult to extract the temperature and species density at a radius of 7.5 mm. The curve fit routine did not converge due to the low signal to noise level in the spectrum of this low O_2 number density flow. Furthermore, at this location, a second spectral band started to appear at 8 nm below the oxygen line which interfered with the curve fit. A manual curve fit procedure was used to fit the spectrum in this case. However, this resulted in less accuracy. Since no oxygen was found at radial distances of 10 mm or greater, the temperature could not be determined from the oxygen Q-branch and should be obtained from the Raman spectrum of water.

The experimentally measured temperature and oxygen number densities were compared with predictions obtained with the RK/PLUS code. This RK/RPLUS Navier-Stokes prediction was obtained using a finite-volume, explicit, four-stage, Runge-Kutta time-marching procedure to solve the coupled Navier-Stokes and species transport equations.[22] Chemical reactions within the engine and plume flowfields were modeled by an 18-step reaction set involving nine chemical species. Chemical kinetics data for H_2/O_2 combustion were based on those from H_2/air in the R-PLUS, LU-SSOR code[23] developed at NASA Lewis for scramjet combustors and applied to the reacting flow within the H_2/O_2 thruster by setting the concentrations of inert nitrogen to zero. Thermodynamic transport properties such as specific heat, dynamic viscosity and thermal conductivity for each species were evaluated as fourth-order polynomials in temperature. These polynomial coefficients, as well as the mixing rules used to evaluate thermodynamics properties of the fluid mixture, were also obtained from the R-PLUS code.

The inlet boundary conditions to this calculation were set as follows. The three-dimensional, radial injection of hydrogen into the flow of oxygen in the core region of the injector was modeled as a uniform, perfectly mixed equilibrium mixture of hydrogen and oxygen for lack of a better estimate. The CEC code[24] was used to determine species composition and temperature in the core flow corresponding to equilibrium conditions for H_2 and O_2 at a mixture ratio of 20.0 and pressure of 453 kPa. The surrounding fuel film cooling flow from the splined sleeve insert was modeled by the injection of pure hydrogen along the chamber walls: 75% of the fuel was specified as film coolant and entered the chamber through an annulus which comprised approximately 16% of the overall inlet area.

The inlet boundary conditions consisted of a specification of propellant mass flowrates, chemical species mass fractions and total enthalpy, while a method of characteristics (M.O.C.) procedure was used to extrapolate the upstream running characteristic variable from within the domain. Specification of propellant mass flowrate permitted direct comparison with test stand conditions and the prediction of engine chamber pressure. The engine walls were assumed to be adiabatic and non-catalytic. Thus, zero normal gradients in temperature and species mass fraction were specified at the walls along with zero normal pressure gradient and no-slip velocity conditions.

To facilitate the solution procedure, the computational domain was divided into two sections: the combustion chamber (including the throat and shortened nozzle) and the near-plume region. Flow quantities (density, velocity, total energy per unit mass and species mass

fractions) at an axial location downstream of the throat (where the flow is fully supersonic) were used to specify supersonic inlet conditions for the plume flowfield. At supersonic inlet boundaries, all flow quantities were specified.

The computational domain for the near-plume flowfield was a semi-circular region centered at the nozzle exit plane and having a radius of approximately one and a half exit plane diameters. A viscous, no-slip condition was applied to the plume flowfield boundary beyond the nozzle wall parallel to the nozzle exit plane. A supersonic exit boundary condition in which all flow quantities were extrapolated from within the domain was specified along the far-field boundary of the plume flowfield. This condition corresponded to a situation where the engine is exhausting into a vacuum space(i.e. zero back pressure and no entrainment of fluid from within the test chamber). Facility backpressure effects were not modeled.

Figure 6 shows the experimentally measured temperature at $z=10$ mm and compares it with predictions for the $z=0$ mm and $z=10$ mm planes. Two features stand out in the comparison between the experimental and numerical results. The measured temperature was higher than the calculated temperature by 150-250 K (10 to 15%). Both predicted and measured temperature profiles at this axial station reveal similar flow structure, specifically the presence of a local maximum in temperature at some radial distance from the centerline. The predicted profile subsequently shows a decrease. Since no oxygen was present beyond 10 mm radius, no experimental data were obtained to verify this.

Isotherms and isobars for this engine flow field as predicted by RK/PLUS are shown in Fig. 7. The narrow region of temperature increase caused by reactions in the shear layer have roughly the same spatial location in the exit plane as a weak compression wave originating at an inflection point in the shortened nozzle contour. Schlieren visualization failed to verify the presence of such a wave, probably due to the weakness of the compression wave combined with the low number density and three dimensional nature of the plume flow.

However, the two effects propagate downstream in different directions. The compression wave acts as a very weak oblique shock and propagates towards the centerline. The high temperature combustion products from the shear layer travel with the expanding gas and move away from the centerline. The computed temperature profile at the $z=10$ mm plane in Fig. 6 shows this compression wave as a small bump at approximately 5 mm radius, slightly inward from the peak in the exit plane, while the mixing layer appears as a weak bump at approximately 12 mm.

The measured O_2 number density profile at the $z=10$ mm plane is shown in Fig. 8. The measured profile is much steeper in the radial direction than predicted. To establish the effect of the facility geometry on the measured O_2 concentration profile, the numerically predicted profile of the oxygen number density in the exit plane is also plotted (dashed line) in Figure 8. The measured O_2 number density profile at $z=10$ mm downstream of the exit plane actually lies much closer to the predicted exit plane number density profile than to the predicted number density profile at $z=10$ mm downstream. The slower expansion in the experimental configuration than in the numerical analysis is a likely contributor.

Discussion

As actual experimental core flow inlet conditions are unknown for input to the calculation domain and the splitter plate recirculation zone has not been modeled, it is probable that the small increase in experimentally measured temperature with increasing radius is caused by the secondary combustion in the reacting shear layer rather than a weak compression wave. Previously described facility effects limit expansion downstream of the exit plane and, as a result, the region of increased temperature should diverge less than predicted from the centerline.

To establish whether the facility geometry has an effect on the measured profiles, the calculated temperature profile at the exit plane, $z=0$ mm, is also plotted in Fig. 6 (dashed line). This exit temperature profile was much less dependent on facility effects. A distinct sharp peak off the centerline can be seen, caused by the way that the code models the reaction in the mixing layer inside the combustion chamber and by the existence of the compression wave. The peak is sharp and narrow. This indicates a thin mixing layer with limited diffusion is computed in the combustion chamber. These data agree with other measurements[5,7] showing that the degree of mixing in the shear layer is underpredicted by the RK/PLUS code.

The higher measured temperature across the full measured profile relative to the predictions can partly be attributed to facility effects. Numerical results are for a free expansion into a vacuum, where boundary conditions allow the expanding flow to attach to the endplate of the shortened rocket. Accordingly, the axial temperature decrease will be greater at the z=10 mm plane in this numerically predicted plume than in the experimental plume, where the back pressure and the presence of the diffuser tends to limit the rate of expansion.

This 10-15% difference between measured and predicted temperatures result, in addition to the effects discussed above, from the experimental method used. The spectral prediction calculates each rotational vibrational line and their relative magnitudes. Since the current approach is based on full thermodynamic equilibium, the translational, rotational and vibrational temperatures are assumed to be equal. Because of the small Raman shift for oxygen and the large number of rotational levels, all rotational lines are extremely close together. Using a relatively broad band laser to excite the molecules completely obscures the rotational structure and only vaguely shows the vibrational structure. The curve fit for the oxygen spectrum is dominated by the vibrational structure. Therefore one can assume that the temperature measured is the vibrational temperature.

Thus an inherent assumption of the technique is that vibrational and rotational temperatures are equal. To verify the validity of this assumption it is necessary to estimate the relaxation times associated with translation, rotation, and vibration. Since the core is oxygen rich, the dominant collision partner was assumed to be oxygen and collisions with water and minor species were neglected. The measured oxygen partial pressure on the centerline was 45 kPa. This is the total pressure, assuming oxygen was the only species present. The measured temperature was approximately 2050 K. The viscosity of oxygen at 2000 K is approximately 723×10^{-6} gm/(cm.sec), giving a mean free path of oxygen of about 1.4×10^{-7} cm. The translational relaxation time can be calculated from:[25]

$$\tau_{tr} = \lambda_{tr} \sqrt{\frac{\pi m}{8 k T}} \qquad (1)$$

Using this equation where m is the molecular mass of oxygen and λ_{tr} is the mean free path length of oxygen, we find a translational relaxation time of 1.1×10^{-7} sec. No such simple expression is available for the rotational relaxation but rotational relaxation is slightly slower than translational relaxation. At these temperatures, they are very close. Accordingly, rotational relaxation rates are of the order 10^{-6} - 10^{-7} seconds.

The calculated velocity at the probe volume is of the order of 2000 m/s, which means that the gas moves approximately 0.2 and 1 mm before translational and rotational equilibration, respectively. With the probevolume diameter of approximately 0.8 mm, translational and rotational equilibrium can be assumed.

Vibrational relaxation can be calculated from:[25]

$$\tau_{vib} = C_{vib} \frac{\exp(K_2 / T)^{1/3}}{p} \qquad (2)$$

where the constants $C_{vib} = 5.42 \times 10^{-5}$ atm-μsec and $K_2 = 2.95 \times 10^6$ K for oxygen with oxygen as the collision partner. For the test conditions, this gives a vibrational relaxation of 1.1×10^{-5} sec. During vibrational equilibration, the gas moves approximately 20 mm. The conditions for vibrational equilibrium clearly have not been met.

Since the temperature measured is the vibrational temperature, and it takes the vibrational energy much longer to equilibrate than translation and rotation, the temperatures measured here are higher than the total gas temperature at this location. This is a contributor to the discrepancy between experimental and numerical results. To obtain a quantitative estimate of the difference between vibrational temperature and flow temperature it would be necessary to follow the gas volume that passes through the probe volume from upstream of the throat up until it reaches the probe volume and to study its evolution.

The discrepancy in measured and predicted oxygen number density and its radial gradient at the z=10 mm plane is likely due to several effects which concur with the discussion of the temperature measurements above. The core flow inlet boundary conditions were unknown for input to the calculation domain and any lack of mixing in the core would result in an increase in O_2 number density over that predicted. The splitter plate

recirculation zone, which was not modeled, would experimentally cause mixing between the core flow and film, consuming more O_2 in the shear layer than predicted. Facility back pressure effects limit expansion downstream of the exit plane and as a result the O_2 concentration diverges less than predicted from the centerline.

Based on the results presented here, some preliminary conclusions can be drawn on the mixing efficiency of this design and the modeling used. The measured oxygen profile indicates a strongly stratified reaction region in the injector. Shear layer mixing and accompanying secondary combustion do not appear to have much effect on this stratification. It is likely that not much hydrogen is being entrained in the recirculation zone behind the sparkplug tip shown in Fig. 1, resulting in a stratified injector exit flow composed of a core of almost pure oxygen and a tube of combustion products. As the thermal velocity of the hydrogen inside this region is large, fast cross flow diffusion, combined with turbulent mixing will cause better mixing and combustion just downstream of the sparkplug tip. However, this is largely confined to the outer layers of the core flow as reflected in the measurement of the high oxygen number density at the center line and the large gradient in the radial direction. All hydrogen in the core section will be consumed before it reaches the center. Measurements at the exit of the fuel film sleeve insert are necessary to confirm this. In the main chamber, this core flow forms a shear layer with the hydrogen film at the exit of the fuel film sleeve. Since the combustion process in this region is turbulent mixing dominated, limited combustion occurs in this secondary reaction region during the reactant residence time in the combustor. This secondary combustion in the shear layer is further reduced by the limited number of oxygen molecules available in the outer layer of the oxygen rich core, leading to a relatively poor mixing efficiency.

These results show that any modeling of the flowfield should include the injector section. Assuming a uniform, perfectly mixed equilibrium mixture as a core flow inlet boundary condition for the computational domain will most likely yield misleading predictions, specifically in the number density profile.

Concluding Remarks

Raman spectroscopy has been successfully implemented to measure the near exit major species density and temperature of a 110 N gaseous hydrogen/oxygen rocket. Optical fibers were used for both laser beam delivery and signal acquisition. Together with the high pulse energy of the pumped dye laser, this system allowed a wide range of number densities to be measured and a great flexibility of measurement location. For the low number densities in a rocket plume, a photomultiplier tube with a high quantum efficiency is the detection device of choice even though 2-D arrays would increase the speed of data acquisition. Efforts are underway to determine the lower limit of measurable number densities with a non-intensified array over the spectral range of choice.

Oxygen number densities as low as 10^{17} /cm^3 have been measured in the plume. Some discrepancies are observed in the comparison between measured O_2 number densities and those predicted using an axisymmetric Navier-Stokes (RK/PLUS). The comparison shows a significantly steeper measured oxygen gradient in radial direction than predicted. The predictions also indicate an oxygen rich plume core flow which expands much faster than experiments show.

The measured temperature profile reveals some of the combustion chamber injection geometry, specifically the presence of the mixing layer. Theoretical predictions at the downstream measurement location do not accurately predict the measured profile. Both the temperature and oxygen number densities profiles show measured profiles which lie in between the profiles predicted at the exit plane and the downstream $z = 10$ mm plane. The discrepancies are mainly attributable to facility and inlet boundary condition effects which have not been accounted for in the model and on the assumption of local thermodynamic equilibrium for the Raman measurement. Improved modeling of the combustion chamber geometry and experimental facility effects should provide closer agreement between measurements and numerical results.

Raman measurements inside the rocket chamber to experimentally set the inlet boundary condition to the computational domain are needed.

Appendix A: Raman Scattering Theory

When light passes through a molecule, its oscillating electric field vector will interfere with the molecular

energy field by disturbing the motion of charged particles within the molecule. As a result, the molecular energy field is distorted and the vibrational motion of the nuclei with respect to the molecular center of gravity is affected. Similarly, due to a change in the moment of inertia, the molecular rotational motion is affected.

The external electric field creates a dipole moment inside the molecule by polarizing the charged particles. The magnitude and direction of the dipole moment created under influence of this electric field depends on a property of the molecule called "polarizability", primarily dependent on the electron orbits (electronic wave functions) and expressed by the tensor α_0. The induced dipole oscillates primarily with the frequency of the incident electric field vector (light) and accordingly radiates light with this incident frequency. No permanent internal energy change occurs to the molecule. This "elastic scattering" phenomenon is referred to as Rayleigh scattering.

A second but much weaker (order of 10^3) light scattering process occurs as the result of the disturbance of the dipole moment caused by the vibrational motion of the molecule. The polarizability of the molecule changes as the result of the internal vibrational motion, the frequency of vibrational motion several orders of magnitude smaller than the incident light frequency. This change in magnitude and direction of the polarizability tensor is given by a secondary tensor α', called the derived polarizability tensor. When the vibrational energy level of the molecule changes through an exchange of energy with the incident electric field, the change in polarizability causes light to be radiated with a frequency dependent on the incident light frequency and on the change in vibrational frequency. This "inelastic" process during which the internal energy state of the molecule changes, is referred to as Raman scattering.
Due to the internal structure of the molecules, only transitions between adjacent vibrational frequencies are possible, given by a change in vibrational quantum number of $\Delta v = \pm 1$ (referred to respectively as Stokes and anti-Stokes scattering). Similarly, rotational changes can occur. The only allowable rotational transitions in Raman scattering are given by the quantum number jumps $\Delta J = 0, \pm 2$.

When monochromatic light (for example a laser source) is incident on a gas volume, the light emitted from this volume is made up distinct frequencies. The strongest line is at the laser line frequency, the Rayleigh scattering. Two weaker bands on either side of this line give are the Raman lines. Since vibrational frequencies and also the difference between adjacent vibrational frequencies within a molecule (referred to as Raman shift) are distinct for each individual species, the location of the Raman lines with respect to the incident laser indicates the gas species contributing to the scattering. The strength of the lines indicate the number densities of the species that undergo the specific rotational vibrational transition.

A gas in thermodynamic equilibrium satisfies the Maxwell-Boltzman distribution. This distribution indicates that at room temperature virtually all molecules reside in the lowest (ground) vibrational state. This excludes the transition $\Delta v = -1$. Therefore, no anti-Stokes line will appear. With increasing temperature, higher vibrational levels become populated, and slowly the anti-Stokes line will become stronger.

At room temperature many rotational levels are well populated. Therefore, all three allowable rotational transitions are possible and show about equal strength. The rotational lines are referred to as the O-, the Q- or the S-branch, according to which transition, $\Delta J = -2,0$ or $+2$ takes place. The O- and S-branch transitions for most species are much weaker than the Q-branch transition.[19] Furthermore, since the lines $\Delta J = -2$ and $+2$ are spread farther apart then the $\Delta J = 0$ line, they are well resolved but often not detectable. Since all lines contributing to the Q-branch are bunched up in a narrow spectral region, they often appear as one (relatively) strong line.

The scattering intensity for each Q-branch transition depends on the laser intensity, the number of molecules in the initial rotational vibrational energy level and the transition probability. The number of molecules in the initial energy level depends on the temperature and is given by the Boltzman distribution. The transition probability can be determined from Placzek's[26] polarizability theory. It depends on the vibrational and rotational quantum numbers. However, Schroetter and Kloeckner[27] show that the transition probability of a rotational-vibrational band is independent of the rotational excitation.

The light intensity observed in an experiment furthermore depends on the experimental geometry and detection equipment. Including these factors, the light

intensity observed is:

$$I_{sc,ob}=C.N_{J,v}.I_{las}.\Omega.(\frac{a\sigma_{Raman}}{d\Omega})_{J,v,\theta} \qquad (A-1)$$

where the factor C includes the length of the probe volume, the optical losses caused by lenses and spectrometer equipment and the detection device quantum efficiency. This factor is system dependent and can be found by calibration. $N_{J,v}$ is the species number density in the initial energy level given by the rotational and vibrational quantum numbers J and v. I_{las} is the incident laser intensity and Ω is the solid angle of the receiving optics (determined by the effective receiving f#). The last term is called the differential Raman scattering cross section[19] and represents the transition probability.

The species number density in the initial state for a mixture in thermodynamic equilibrium is given by the Boltzmann distribution as:

$$N_{J,v}=N.\frac{g_n.(2J+1)}{Z_{J,v}}.\exp(-\frac{E_{J,v,ini}}{k.T}) \qquad (A-2)$$

where N is the total number of the species, g_n is the nuclear degeneracy, which only affects homonuclear molecules, $Z_{J,v}$ is the partition function of the initial distribution, $E_{J,v,ini}$ is the rotational vibrational energy of the initial state, k is Planck's constant and T the absolute temperature.

The Raman scattering cross section represents the transition probabitily between two energy states. The fundamental expression for this cross section is:

$$\sigma_{Raman}=\frac{2^7.\pi^5}{3.c^4}.(\nu_{las}-\nu_{RS})^4.\sum(|\alpha'_{ini,fin}|^2) \qquad (A-3)$$

where ν_{las} is the laser frequency, ν_{RS} is the Raman shift, which is characteristic for each species and represents the energy difference between the initial and final energy states and $\alpha'_{ini,fin}$ is the matrix element of the derived polarizability tensor, which describes the change in polarizability as the consequence of the molecular vibrational motion. The term $|\alpha'_{ini,fin}|^2$ is the transition probability, and the subscripts ini and fin indicate that this term depends on the change in polarizability between the initial and final states.

To solve this equation in more manageable terms is not a trivial task. It depends on the electronic, vibrational and rotational wavefunctions of the initial and final molecular states[28] and on the nature of polarization of the incident radiation. The scattering cross section has the dimension of area. An interpretation is that all the radiation incident on an area equal to this cross sectional area is scattered.

The differential scattering cross section represents the portion of the scattered radiation that is scattered into the angle of observation. Besides the parameters mentioned, it's value also depends on the angle between the incident and observed radiation, the solid angle of observation (in sterradians), the quantum numbers of the initial and final states and the wavelength of radiation. The rotational dependence is given by S_J, the Teller-Placzek coefficient.[28] The vibrational dependence is given by the factor $(v+1)$. The functional dependence of the differential scattering cross section on these parameters is given by:

$$(\frac{d\sigma_{Raman}}{d\Omega})_{J,v} \propto S_J \,.\, (v+1) \qquad (A-4)$$

Measured absolute values of the differential scattering cross section for common species can be found in literature[27] but have to be applied with care since they are commonly determined for a certain incident and scatttered polarization. Depolarization ratios are needed to correct for different geometrical experimental setups and different polarizations.

So far it has not been possible to measure values for short lived species such as intermediates in combustion. For these species, calculations have to be made to determine the approximate cross sections. One approach and computed values for some intermediates has been given by Coll and Melius.[29] They also calculated some values for major species and compared them with measured values.

The Raman shift (difference between two adjacent energy levels) is different for each individual rotational-vibrational transition, due to the difference in

rotational-vibrational coupling and anharmonicity.[28] Consequently, each rotational-vibrational transition scatters at a different frequency, often extremely close in the spectrum. This gives a succession of lines whose linestrengths are given by equation A-1. If a laser can be found with a laser line width smaller than the line separation, and the detection equipment has a resolution better than the line separation, each individual rotational-vibrational line can be resolved. Detection then depends on the detection equipment sensitivity and scattering strength, which depends on the number density of the molecules, the intensity of the incident laser radiation and the solid angle of detection.

References

[1]Byers, D.C., "Advanced Onboard Propulsion Benefits and Status," NASA TM-103174, 1989.

[2]"JANNAF Rocket Engine Performance Prediction and Calculation Manual," CPIA Publication 246, April 1975.

[3]Robinson, P.J., "Space Station Auxiliary Thrust Chamber Technology," NASA Contractor Report 185296 Final Report 2210-90-FR, July 1990.

[4]Richter, G.P., and Price, H.G., "Proven, Long-Life Hydrogen/Oxygen Thrust Chambers for Space Station Propulsion," NASA TM-88822, JANNAF Propulsion Meeting, New Orleans, Aug. 1986.

[5]Weiss, J.M., and Merkle, C.L.,"Numerical Investigation of Reacting Flowfields in Low-Thrust Rocket Engine Combustors," AIAA Paper 91-2080, 1991.

[6]Arrington, L.A., and Reed, B.D., "Comparison of Axisymmetric and Three-Dimensional Hydrogen Film Coolant Injection in a 110-N Hydrogen/Oxygen Rocket," AIAA Paper 92-3390, July 1992.

[7]Seasholtz, R.G., Zupanc, F.J., and Schneider, S.J., "Spectrally Resolved Rayleigh Scattering Diagnostic for Hydrogen-Oxygen Rocket Plume Studies," AIAA Paper 91-0462, July, 1991.

[8]Zupanc, F.J., and Weiss, J.M.,"Rocket Plume Flowfield Characterization Using Laser Rayleigh Scattering," AIAA Paper 92-3351, July, 1992.

[9]Long, D.A., *Raman Spectroscopy*, McGraw-Hill International Book Company, Great Britain, 1977.

[10]Lederman, S.,"The Use of Laser Raman Diagnostics in Flow Fields and Combustion," *Progress in Energy Combustion Science*, Vol.3, 1977, pp 1-34.

[11]Lapp, M., and Penney, C.M.,"Raman Measurements on Flames," *Advances in Infrared and Raman Spectroscopy* (R.H. Clark and R.E. Hester, Ed.), Chapt. 6, Heyden, London, 1977

[12]Lapp, M., "Raman-Scattering Measurements of Combustion Properties," *Laser Probes for Combustion Chemistry* (D.R. Crosley, Ed.), Amer. Chem. Soc. Symp. Series, Vol. 134, Chapt. 17, 1980.

[13]Barlow, R.S., Dibble, R.W., and Lucht, R.P., "Simultaneous measurement of Raman scattering and laser-induced OH fluorescence in nonpremixed turbulent jet flames," *Optics Letters*, Vol. 14, No.5, 1989, pp. 263-265.

[14]Masri, A.R., Bilger, R.W., and Dibble, R.W.,""Fluorescence" Interference with Raman Measurements in Nonpremixed Flames of Methane," *Combustion and Flame*, Vol. 68, 1987, pp. 109-119.

[15]Smith, J.R., "A rotational Raman scattering system for measuring temperature and concentration profiles in transient gas flows," Sandia National Laboratory, SAND-75-2884, 1975.

[16]Wehrmeyer, J.A., Cheng, T-S., and Pitz, R.W., "Raman scattering measurements in flames using a tunable KrF excimer laser," *Applied Optics*, Vol. 31, No. 10, 1992, pp. 1495-1504.

[17]Arrington, L.A., and Schneider, S.J.,"Low Thrust Rocket Test Facility," AIAA Paper 90-2503, 1990.

[18]de Groot, W.A., "The Development of a Fiber Optic Raman Temperature Measurement System for Rocket Flows," AIAA Paper 91-2316, June, 1991.

[19]Eckbreth, A.C., *Laser Diagnostics for Combustion Temperature and Species*, Abacus Press, Cambridge, MA, 1988.

[20]Shirley, J.A., and Chin, D., "Development of Fiber

Optic Raman Diagnostics for SSME Fuel Preburner Temperature Measurements," 1990 Conference on Advanced Earth-to-Orbit Propulsion Technology, NASA Marshall Spaceflight Center, May 1990.

[21]Press, W.H., Flannery, B.P., Teukolsky, S.J., and Vetterling, W.T., *Numerical Recipes: The Art of Scientific Computing*, Cambridge University Press, 1st Ed., Reprint 1990, pp. 524-528.

[22]Weiss, J.M., Daines, R.L., and Merkle, C.L., "Computation of Reacting Flowfields in Low-Thrust Rocket Engines," AIAA Paper 91-3557, Sep. 1991.

[23]Shuen, J.S., and Yoon, S., "Numerical Study of Chemically Reacting Flows Using a Lower-Upper Symmetric Successive Overrelaxation Scheme," *AIAA Journal*, Vol. 27, No. 12, Dec. 1989, pp. 1752-1760.

[24]Gordon, S., and McBride, B.J., "Computer Program for Calculation of Complex Chemical Equilibrium Compositions, Rocket Performance, Incident and Reflected Shocks and Chapman-Jouguet Detonations," NASA SP-273, 1976.

[25]Vincenti, W.G., and Kruger, C.H., *Introduction to Physical Gas Dynamics*, Krieger Pub. Co., Huntington, NY, 1977 Reprint.

[26]Placzek, G.,"Rayleigh-Streuung und Raman-Effekt," *Handbuch der Radiologie, Vol. VI*, (E. Marx, Ed.), Akademische Verlagsgesellschaft, Leipzig, 1934.

[27]Schroetter, H.W., and Kloeckner, H.W., "Raman Scattering Cross Sections in Gases and Liquids," *Raman Spectroscopy of Gases and Liquids* (A. Weber, Ed.) Topics in Current Physics: Springer Verlag, 1979.

[28]Herzberg, G., *Molecular Spectra and Molecular Structure I. Spectra of Diatomic Molecules*, 2nd Ed., Krieger Pub. Co., 1989 Reprint.

[29]Coll, C.F., and Melius, C.F.,"Theoretical Calculation of Raman Scattering Cross Sections for Use in Flame Analysis," Sandia National Laboratory, SAND76-8204, February 1976.

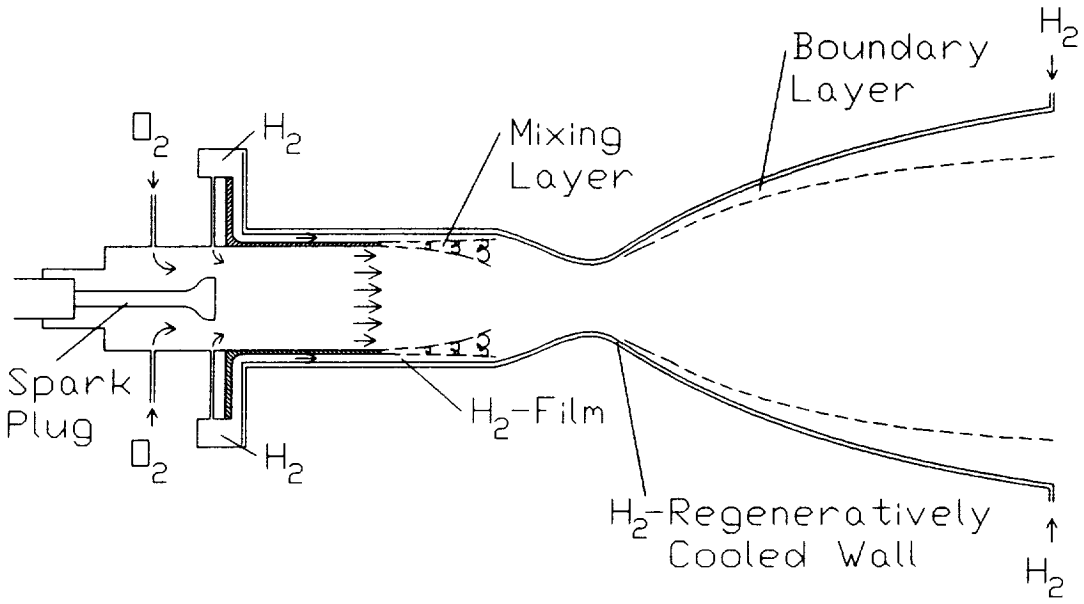

Figure 1: Regeneratively cooled hydrogen-oxygen thruster flowfield with fuel film cooling.

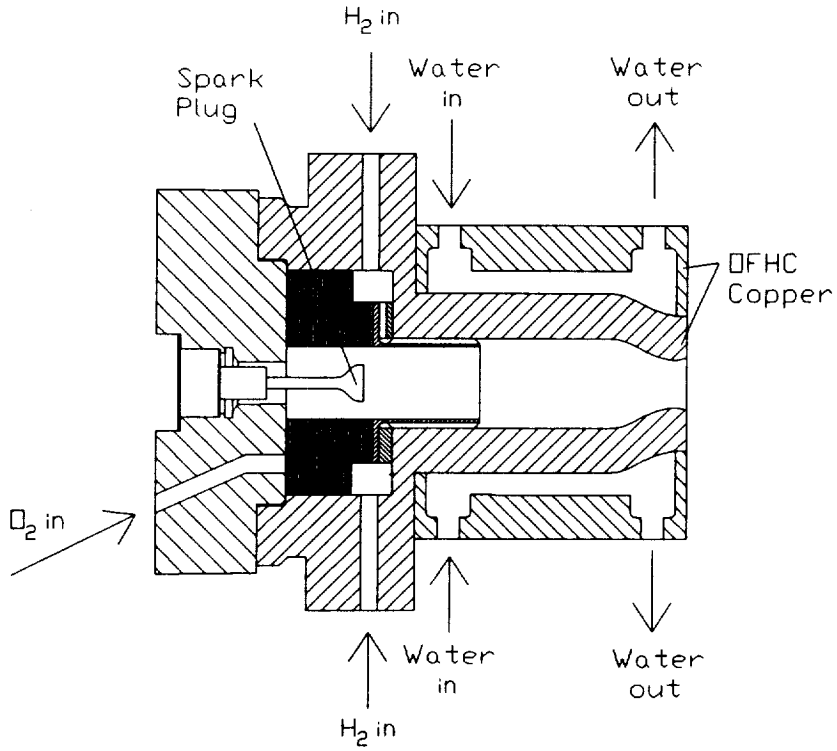

Figure 2: Low area ratio nozzle research rocket.

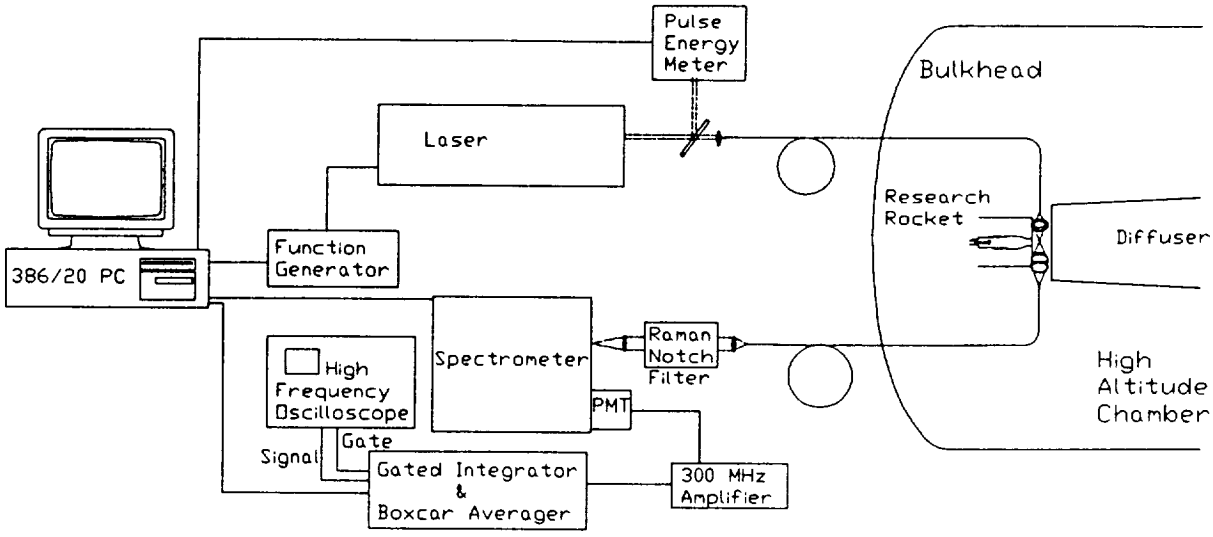

Figure 3: Raman diagnostics facility.

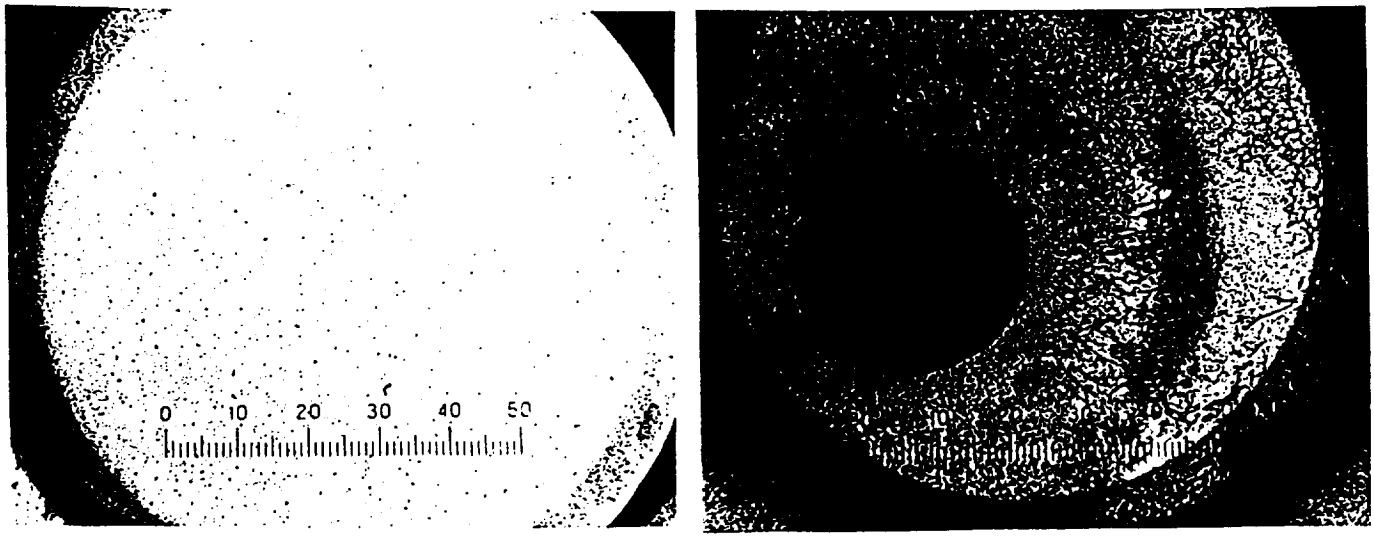

Figure 4: High energy density damage to fiber optics caused by beam focusing on fiber surface. (a) undamaged fiber; (b) misalignment and focusing damage.

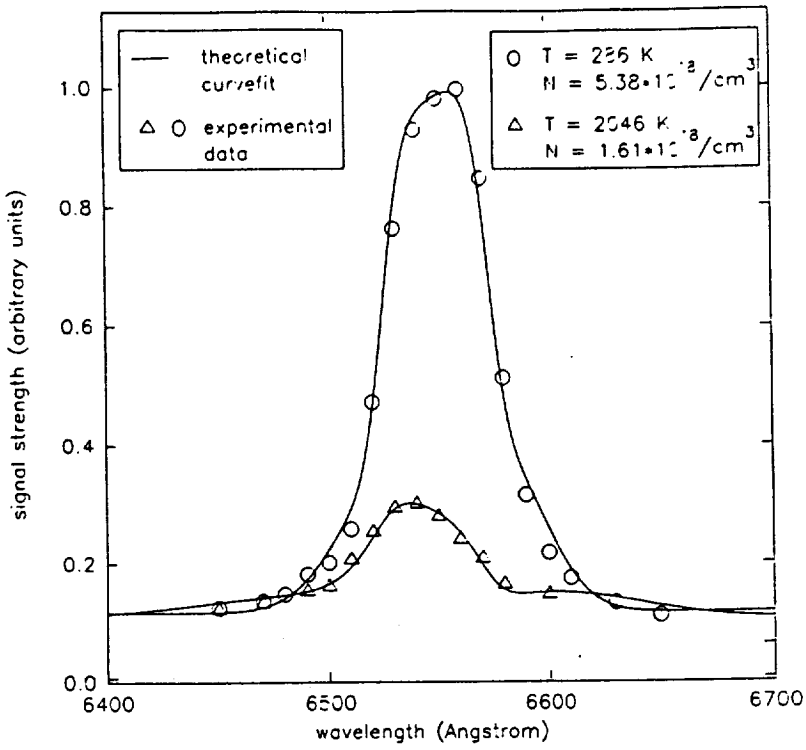

Figure 5: Raman oxygen Q-branch curvefits at different temperatures and number densities.

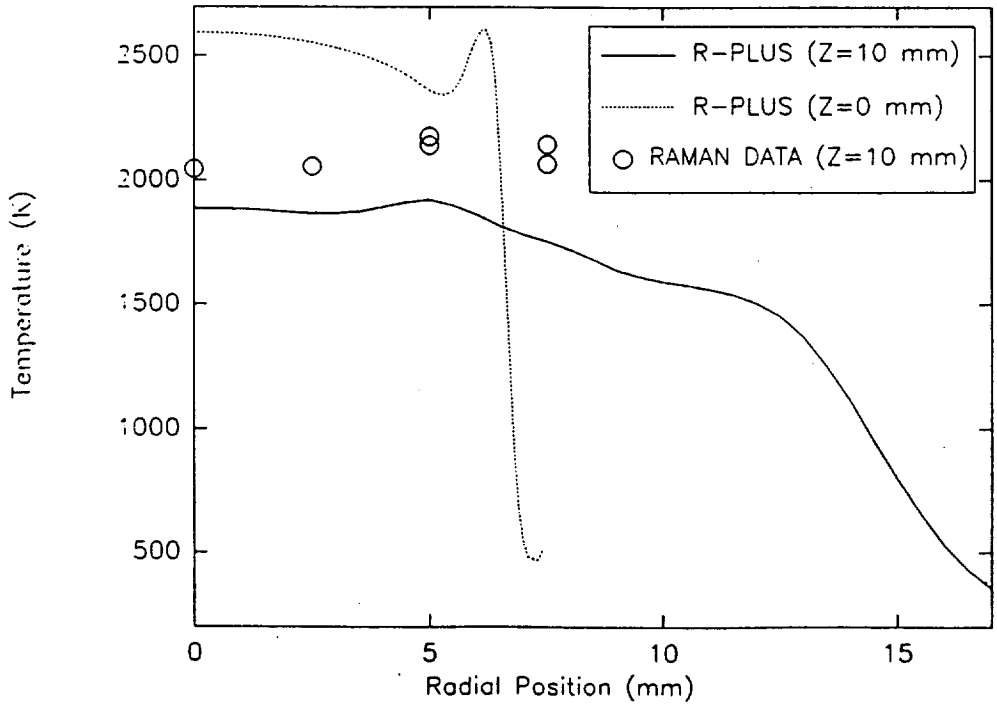

Figure 6: Comparison of Raman temperature measurements in low area ratio nozzle plume with RK/PLUS predictions (O/F=5.0, FFC=75%).

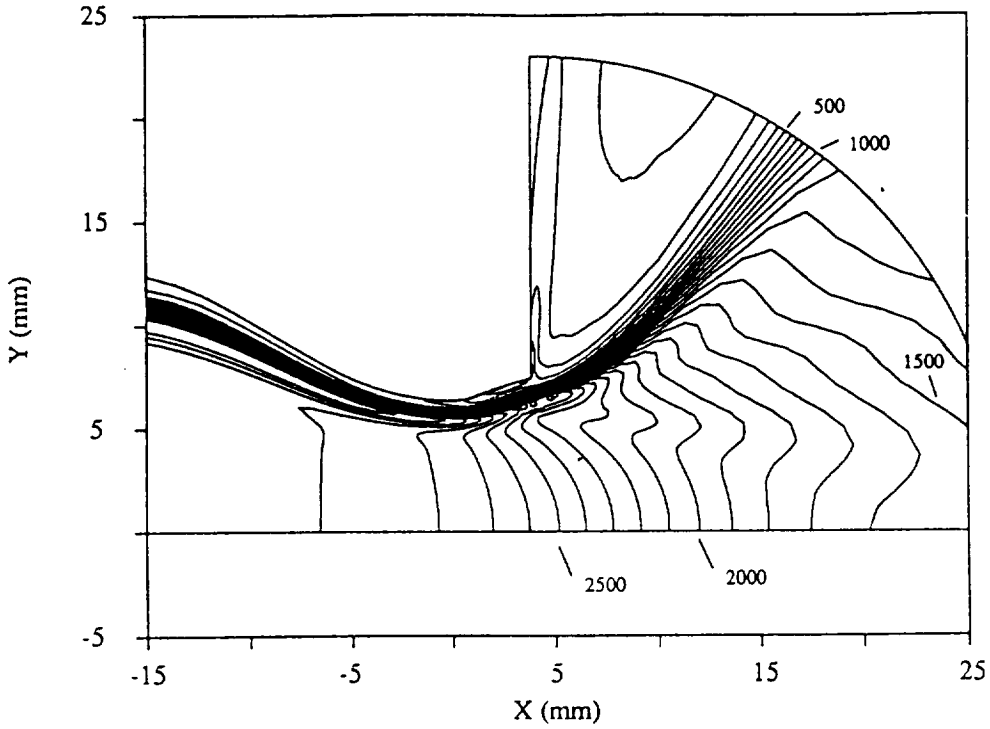

(a) Temperature Contours, delta = 100 K

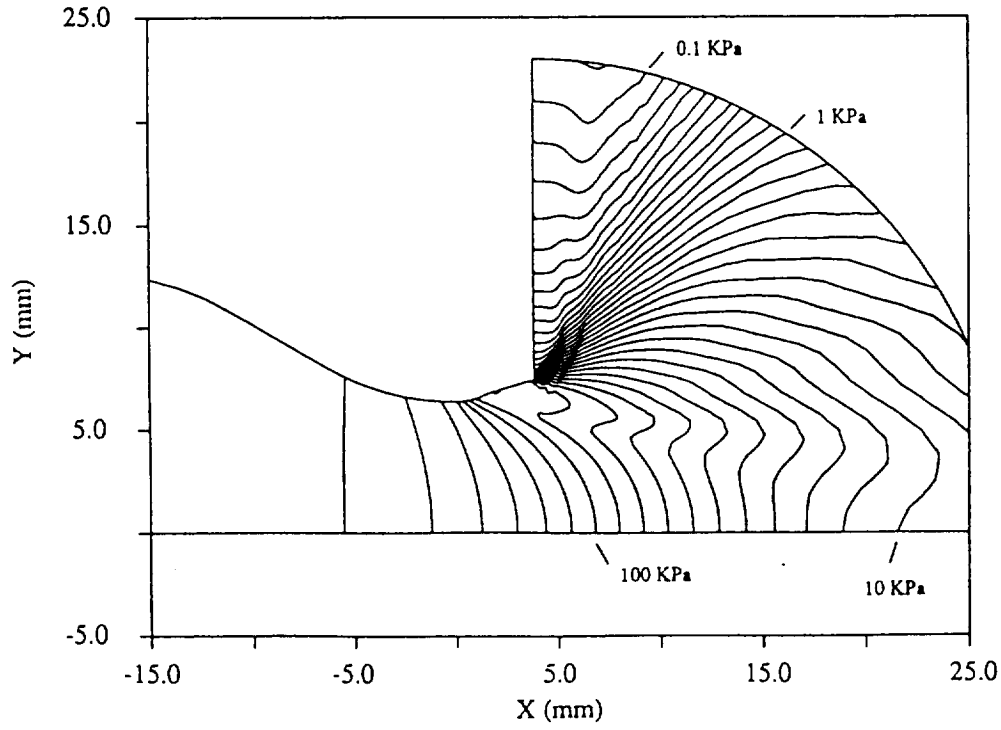

(b) Pressure Contours, delta_log10(P) = 0.1

Figure 7: Isotherms and isobars over the computational domain according to RK/PLUS. (O/F=5.0, %FFC=75) (a) Isotherms; (b) Isobars. (Note: X_{throat}=0.0, X_{exit}-X_{throat}=3.8 mm).

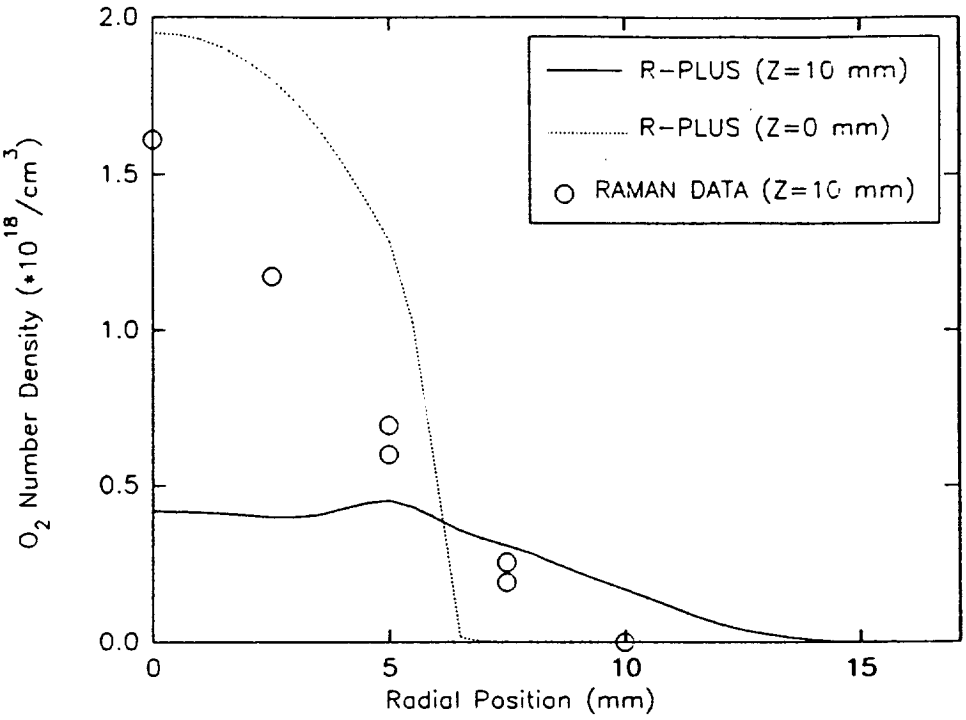

Figure 8: Comparison of Raman measured oxygen number densities in low area ratio nozzle plume with RK/PLUS predictions (O/F=5.0, %FFC=75).

REPORT DOCUMENTATION PAGE

Form Approved
OMB No. 0704-0188

1. AGENCY USE ONLY (*Leave blank*)	2. REPORT DATE	3. REPORT TYPE AND DATES COVERED
	July 1992	Interim Contractor Report

4. TITLE AND SUBTITLE

Species and Temperature Measurement in H_2/O_2 Rocket Flow Fields by Means of Raman Scattering Diagnostics

5. FUNDING NUMBERS

WU–506–42–31

6. AUTHOR(S)

Wim. A. de Groot and Jonathan M. Weiss

7. PERFORMING ORGANIZATION NAME(S) AND ADDRESS(ES)

Sverdrup Technology, Inc.
Lewis Research Center Group
2001 Aerospace Parkway
Brook Park, Ohio 44142

8. PERFORMING ORGANIZATION REPORT NUMBER

E–7246

9. SPONSORING/MONITORING AGENCY NAMES(S) AND ADDRESS(ES)

National Aeronautics and Space Administration
Lewis Research Center
Cleveland, Ohio 44135–3191

10. SPONSORING/MONITORING AGENCY REPORT NUMBER

NASA CR–189217
AIAA–92–3353

11. SUPPLEMENTARY NOTES

Prepared for the 28th Joint Propulsion Conference and Exhibit cosponsored by AIAA, SAE, ASME, ASEE, Nashville, Tennessee, July 6–8, 1992.
Wim. A. de Groot, Sverdrup Technology, Inc., NASA Lewis Research Center Group, 2001 Aerospace Parkway, Brook Park, Ohio 44142.
Jonathan M. Weiss, Propulsion Engineering Research Center, Department of Mechanical Engineering, The Pennsylvania State University, University Park, Pennsylvania 16802. Responsible person, Steven S. Schneider, (216) 433–7484.

12a. DISTRIBUTION/AVAILABILITY STATEMENT

Unclassified - Unlimited
Subject Categories 72 and 20

12b. DISTRIBUTION CODE

13. ABSTRACT ***(Maximum 200 words)***

Validation of Computational Fluid Dynamic (CFD) codes developed for prediction and evaluation of rocket performance is hampered by a lack of experimental data. Non-intrusive laser based diagnostics are needed to provide spatially and temporally resolved gas dynamic and fluid dynamic measurements. This paper reports the first non-intrusive temperature and species measurements in the plume of a 110 N gaseous hydrogen/oxygen thruster at and below ambient pressures, obtained with spontaneous Raman spectroscopy. Measurement at 10 mm downstream of the exit plane are compared with predictions from a numerical solution of the axisymmetric Navier-Stokes and species transport equations with chemical kinetics, which fully model the combustor-nozzle-plume flowfield. The experimentally determined oxygen number density at the centerline at 10 mm downstream of the exit plane is four times that predicted by the model. The experimental number density data fall between those numerically predicted for the exit and 10 mm downstream planes in both magnitude and radial gradient. The predicted temperature levels are within 10 to 15% of measured values. Some of the discrepancies between experimental data and predictions result from not modeling the three dimensional core flow injection mixing process, facility back pressure effects and possible diffuser-thruster interactions.

14. SUBJECT TERMS

Raman scattering; Fiber optics; H_2O_2 rocket flows

15. NUMBER OF PAGES

20

16. PRICE CODE

A03

17. SECURITY CLASSIFICATION OF REPORT	18. SECURITY CLASSIFICATION OF THIS PAGE	19. SECURITY CLASSIFICATION OF ABSTRACT	20. LIMITATION OF ABSTRACT
Unclassified	Unclassified	Unclassified	